nature materials

ARTICLES

https://doi.org/10.1038/s41563-021-00960-1

Check for updates

Phonon renormalization in reconstructed MoS_2 moiré superlattices

Jiamin Quan[1,5], Lukas Linhart[1,2,5], Miao-Ling Lin[3], Daehun Lee[1], Jihang Zhu[1], Chun-Yuan Wang[1], Wei-Ting Hsu[1], Junho Choi[1], Jacob Embley[1], Carter Young[1], Takashi Taniguchi[4], Kenji Watanabe[4], Chih-Kang Shih[1], Keji Lai[1], Allan H. MacDonald[1], Ping-Heng Tan[3]✉, Florian Libisch[2]✉ and Xiaoqin Li[1]✉

In moiré crystals formed by stacking van der Waals materials, surprisingly diverse correlated electronic phases and optical properties can be realized by a subtle change in the twist angle. Here, we discover that phonon spectra are also renormalized in MoS_2 twisted bilayers, adding an insight to moiré physics. Over a range of small twist angles, the phonon spectra evolve rapidly owing to ultra-strong coupling between different phonon modes and atomic reconstructions of the moiré pattern. We develop a low-energy continuum model for phonons that overcomes the outstanding challenge of calculating the properties of large moiré supercells and successfully captures the essential experimental observations. Remarkably, simple optical spectroscopy experiments can provide information on strain and lattice distortions in moiré crystals with nanometre-size supercells. The model promotes a comprehensive and unified understanding of the structural, optical and electronic properties of moiré superlattices.

In vertical van der Waals homo- or heterobilayers with weak interlayer coupling, a finite twist angle between layers leads to a moiré superlattice that induces periodic modulations of atomic structure, energy and optical selection rules[1,2]. Controlling the twist angle with ~0.05–0.1° accuracy[3] in graphene bilayers near the magic angles leads to completely different correlated electronic phases including superconductivity[4,5], orbital magnetism[6,7] and correlated insulator states[8]. Similar phenomena have been observed in transition metal dichalcogenide (TMD) twisted bilayers (TBLs)[9–11], although with a reduced sensitivity to the twist angle[12,13]. In WSe_2 TBLs, correlated insulating states are observed over a broad range of twist angles between 4° and 5.1°, indicating intriguing changes over a magic twist angle continuum[13].

Those prior experiments on moiré superlattices have been interpreted using a rigid lattice model in which the local atomic stacking is assumed to be determined by rotating pristine two-dimensional (2D) lattices. However, theoretical studies and microscopy experiments have shown that substantial lattice relaxation can occur in TMD TBLs[14–18]. Recent piezoresponse force microscopy (PFM) and scanning transmission electron microscopy (STEM)[17,18] measurements reveal a tessellated pattern of mirror-reflected triangular domains in TMD TBLs, separated by a network of thin domain boundaries for twist angles $\theta < 2°$. This precise structural information challenges the interpretations of previous experiments based on a rigid lattice picture.

In this work, we reveal an intricate connection between phonon spectra and moiré lattice reconstruction. Our discoveries are enabled by Raman measurements on a series of MoS_2 TBLs with precisely controlled twist angles and by a theoretical approach for calculating moiré phonons. With increasing twist angle, reconstructed moiré lattices can be categorized into three different regimes. In the relaxed ($0° \leq \theta < 2°$) and rigid ($\theta \geq 6°$) regimes, the Raman spectra hardly change with the twist angle. In the transition regime ($2° \leq \theta < 6°$), however, low-frequency interlayer shear (S) and layer breathing (LB) modes evolve rapidly with twist angle. This evolution is driven by lattice reconstruction and ultra-strong coupling of different phonon modes. We further attribute a splitting of the commonly observed high-frequency intralayer E_{2g} mode to the local distortion of the hexagonal lattice within each monolayer. The excellent agreement between experiment and theory allows us to unambiguously identify phonon hybridization in the 'magic continuum' angle range. In the big picture, we thus open an important 'phonon' perspective on recently observed strong correlation physics in TMDs. By measuring and analysing moiré-scale wavelength phonons, we show that these degrees of freedom have their own unique moiré physics.

Atomic reconstruction in twisted bilayers

The atomic reconstruction of the moiré pattern is determined by a twist-angle-dependent competition between strain and interlayer coupling[15,17,19–21], as shown in Fig. 1 (Supplementary Discussion I for detailed calculation). At small twist angles, the real space supercell is very large, allowing substantial lattice relaxation even though it is driven by weak van der Waals interactions between the layers and inhibited by strong in-plane bonding within each layer. The relaxation pattern forms large triangular regions in which the energetically favourable stacking configurations (Fig. 1c right column and Supplementary Discussion I) known as AB(BA) stacking (or 3R stacking for $\theta = 0°$; Supplementary Discussion II) are approached[15,22]. The local strain (left column in Fig. 1c) in the relaxed regime peaks along domain boundaries and at topological defects[23] with AA stacking where domains intersect.

As the twist angle increases and real space supercell size decreases, the distance between neighbouring AB and BA stacking

[1]Department of Physics, The University of Texas at Austin, Austin, TX, USA. [2]Institute for Theoretical Physics, Vienna University of Technology, Vienna, Austria. [3]State Key Laboratory of Superlattices and Microstructures, Institute of Semiconductors, Chinese Academy of Sciences, Beijing, China. [4]National Institute for Material Science, Tsukuba, Japan. [5]These authors contributed equally to this work: Jiamin Quan, Lukas Linhart. ✉e-mail: phtan@semi.ac.cn; florian.libisch@tuwien.ac.at; elaineli@physics.utexas.edu

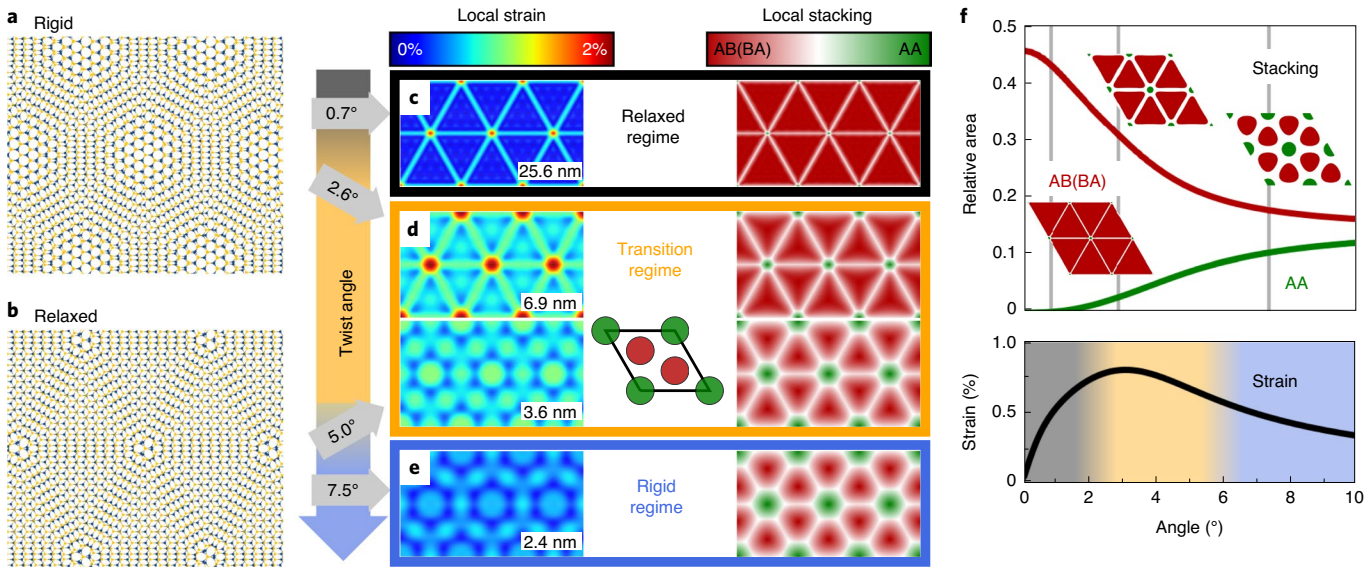

Fig. 1 | Twist-angle-dependent lattice reconstruction in MoS_2 TBLs with small twist angles. a,**b**, Two rotated layers of MoS_2 without (**a**) and with (**b**) lattice relaxation (exaggerated for clarity). **c**–**e**, Calculated patterns of local strain (left column) and stacking (right column) at various twist angles. The plots are drawn in moiré cell units to facilitate comparison of quasi-periodic supercells of different sizes. Three distinct lattice reconstruction regimes can be identified: the relaxed regime (black rectangle, **c**), the transition regime (orange rectangle, **d**) and the rigid regime (blue rectangle, **e**). The inset illustrates the area of AA (dark green) and AB(BA) (dark red) stacking within a rigidly rotated bilayer. **f**, The top shows the fraction of the total area covered by AB(BA) (dark red) or AA (dark green) stacking. Area is counted as AA/AB(BA) if the relative displacement between the layers is smaller than 0.25 times the lattice constant. The insets represent three representative lattice stackings corresponding to twist angles at 0.7°, 2.6° and 7.5° (grey lines). The bottom shows the evolution of the average (local) strain in the system (exact definition as in Supplementary Discussion I).

configurations is reduced (Fig. 1d). Correspondingly, the area occupied by the domain walls that interpolate between them increases steadily across a transition regime. Finally, the TBL reaches the rigid regime at large twist angles ($\theta \geq 6°$). In this regime (Fig. 1e), the area with nearly perfect low-energy and high-symmetry AB(BA) stacking is small. The resulting reduction of strain leads to essentially flat[24] rigid layers[15,25]. The evolution of the low-energy AB(BA) area (red line) and the high-energy AA area (green line) as a function of twist angle is summarized in Fig. 1f (top), while the area-averaged strain is summarized in Fig. 1f (bottom). These variations of atomic configuration and local strain are expected to modulate the lattice vibrations.

Strain and coupled phonons observed by Raman spectroscopy

We measured Raman spectra from a series of MoS_2 TBLs with accurately controlled twist angles in the range $0° \leq \theta \leq 20°$. Details of the sample preparation procedure and Raman measurements are discussed in the Methods and Supplementary Discussion III. The measured spectra feature several phonon modes divided into the low-frequency (Fig. 2a) and high-frequency ranges (Fig. 2b). The low-frequency Raman spectra exhibit two types of phonon modes, the interlayer S and LB modes, in which the relative motion of the two monolayers is parallel or perpendicular to the 2D layers, respectively[26–29] (Fig. 2a top). These two types of phonon modes are identified based on their distinct polarization dependence in polarization-resolved Raman measurements. The LB Raman modes have a fine structure due to coupling to discrete LB modes of the hexagonal boron nitride (hBN) substrate with a finite thickness[30] (Supplementary Discussion V). We remove this fine structure[30] (Supplementary Fig. 6) to focus on the main features related to moiré pattern reconstruction via a fast Fourier transform filter (Supplementary Discussions VI and VII). As the twist angle increases, one branch of the LB mode (LB_1) blueshifts and seems to disappear along with the S mode, while a second branch of the LB mode (LB_2) emerges. In the high-frequency Raman spectra there are two dominant intralayer modes (Fig. 2b), commonly denoted as E_{2g} (385 cm^{-1}) and A_{1g} (407 cm^{-1}) following the assignments appropriate for the D_{6h} symmetry of bulk (2H stacked) MoS_2 (refs. [31,32]). The two-fold degenerate E_{2g} mode originates from opposite motions of two sulfur atoms relative to the Mo atom within the 2D plane, while the A_{1g} mode arises from the out-of-plane relative vibrations of the sulfur atoms[31,33] (Fig. 2b top). Although the A_{1g} mode frequency is nearly independent of twist angle, the E_{2g} mode evolves into a doublet in the $2° \leq \theta < 6°$ transition regime, which we will discuss in more detail below. While Raman measurement on TMD TBLs has previously been reported[24,34–37], those experiments were performed on samples with much less control of twist angle and missed the systematic phonon renormalization captured by our experiments.

The evolution of the Raman spectra is further analysed by tracking the peak positions and linewidths as a function of twist angle (Fig. 3a–c). Distinct features emerge in the three regimes. In the relaxed regime ($0° \leq \theta < 2°$), the frequencies and linewidths of all modes exhibit little change because the moiré patterns remain qualitatively the same (matching the $\theta = 0°$ case[26]) with only quantitative changes in the AB(BA) domain area. In the transition regime ($2° \leq \theta < 6°$), the phonon spectra change drastically. The S mode broadens and quickly disappears. There is also a rapid and systematic change in the frequency and intensity (Supplementary Discussion IX). Prominently, the evolution of the LB modes resembles an anticrossing behaviour (Fig. 3a) typically observed when hybrid modes form due to coupling between different phonon modes, as we explain below. The linewidth of each phonon mode directly reflects the phonon lifetime. Assuming[38] that the linewidth γ is related to the lifetime τ by $\tau = \hbar/\gamma$, where $\hbar$ is the reduced Planck's constant, we find that the lifetime of the LB_1 mode is 49 ps and 7.1 ps for TBLs at 2° and 3.3°, respectively. These drastic changes in phonon frequency and lifetime in the transition regime may be

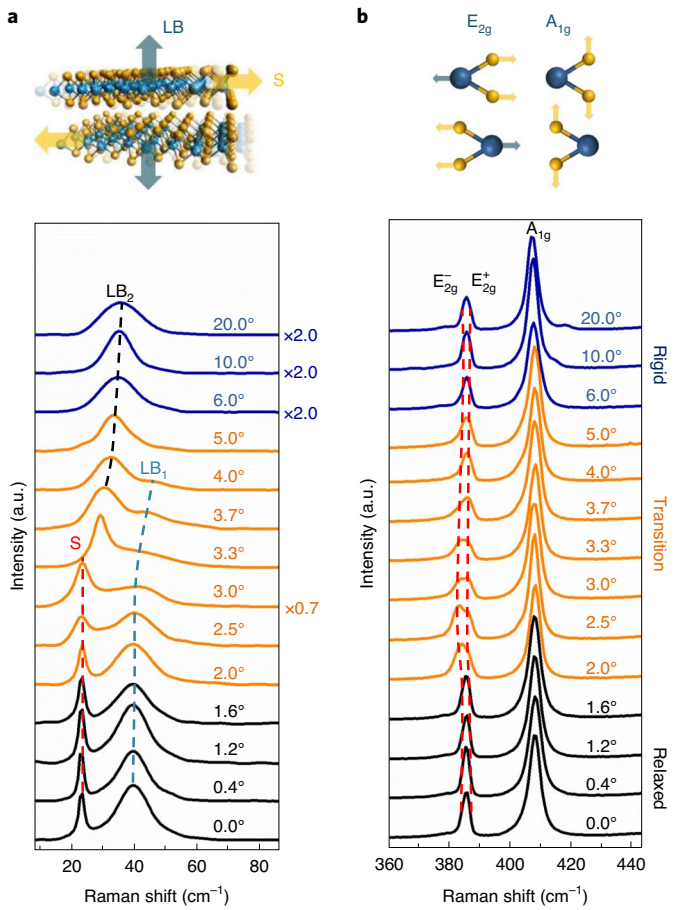

Fig. 2 | Measured Raman spectra of MoS_2 TBLs as a function of twist angle. **a**, Interlayer phonon modes including the S mode and two LB modes (LB_1 and LB_2). **b**, Intralayer phonon modes and the measured Raman spectra including the two E^+_{2g} (E^-_{2g}) modes and one A_{1g} mode. The spectra are scaled and offset for clarity and the scale factors are shown on the edge of the panel; note that scale factors of 1.0 are omitted. The illustrations at the top show the schematic diagrams of the atomic eigenvectors for each phonon mode. The S mode (LB modes) corresponds to in-plane (out-of-plane) relative motions of the constituent layers; the E_{2g} mode corresponds to in-plane relative motion between molybdenum and sulfur atoms; and the A_{1g} mode corresponds to out-of-plane sulfur atom vibrations.

used to infer twist angle and supercell size on the basis of the TBL Raman spectra alone, offering a simple and powerful spectroscopy technique to characterize moiré crystals. The onset of the transition regime identified by Raman spectra at θ of ~2° agrees remarkably well with a very recent STEM study performed on mechanically stacked MoS_2 TBLs[17]. Finally, in the rigid regime with $\theta \geq 6°$, incommensurate stacking again results in stable Raman spectra with little dependence on the twist angle. In this regime, the exponential dependence of the polarizability on the layer separation substantially reduces the intensity of the S mode, explaining why it is not observed in our experiments[24,34,35] (Supplementary Discussion X).

Clear signatures of three reconstruction regimes are also found in the high-frequency E_{2g} mode (Fig. 3c). In the relaxed regime, strain is absent except on the sharp domain walls. Since domain walls only account for a small fraction of the total sample area in the relaxed regime, their influence is not observed in our far-field measurements but may be revealed in near-field measurements[14]. Meanwhile, strain is too small in the rigid regime. Thus, no clear peak splitting is observed in either of these two regimes. By contrast, the mode splits into a doublet E^+_{2g} and E^-_{2g} in the transition regime due to local strain caused by the atomic reconstruction. High strain locally distorts the hexagonal unit cell and breaks the three-fold rotational symmetry, ultimately causing the E_{2g} mode to split[39,40] (Fig. 3d). Based on a two-peak fitting (Supplementary Discussion VI), the largest splitting of the E_{2g} mode, up to 3.2 cm^{-1}, occurs at the $\theta = 2.5°$ TBL, where the influence of strain on hexagonal symmetry is maximal (Fig. 1f bottom). Notably, our measurements report averaged strain under the laser spot. Local variations of strain within a moiré supercell can be resolved using a near-field technique[14]. However, reaching a sufficient spatial resolution in the transition regime, where the supercell size ranges from 9 nm (2°) to 3 nm (6°), would be very challenging. Previous Raman spectroscopy experiments on TBLs[24,35,41–46] with less accurate twist angle control have focused on the electronic enhancement of the Raman signal or on moiré folded phonons. They have been explained via pristine cell calculations[26], simple zone folding[41] and effective force constant models[30]. While twist-angle-dependent phonon modes have been predicted in supercell calculations[42,47], their relation to lattice reconstruction and mode hybridization[48] has not been observed experimentally.

We confirm the presence of atomic reconstructions in a TBL at a θ of ~0.08° by PFM measurements. The large strain gradients near the AA stacking regions and the domain walls (Fig. 1c–e) allow piezoelectric coupling to an out-of-plane a.c. electric field[18] (Methods). PFM data in Fig. 3e clearly reveal the reconstructed moiré superlattice with a typical size of ~230 nm as expected. The superlattice is divided into large triangular AB/BA domains by narrow domain walls that locally break the single-layer D_{3h} symmetry (Fig. 3d). The results confirm the high quality of our samples and the expected moiré reconstructions in the relaxed regime.

A continuum model to understand phonon renormalization

Simple models such as phonon dispersion folding[41] or force constant models[27,30,42] previously developed to describe Raman experiments in bilayers cannot explain the complicated evolution of modes we observe. Full ab initio calculations become too expensive at small twist angles[24] and are, like effective force constant models of supercells[47], limited to commensurate twist angles (Fig. 4a). Here, we adapt a low-energy continuum model approach, developed by Bistritzer and MacDonald[49,50], to calculate the electronic system of moiré superlattices, to phonons in TBLs (Supplementary Discussion XI for details). The pristine lattice vectors $\mathbf{a}_1 = (a_0, 0)$, $\mathbf{a}_2 = a_0(-1, \sqrt{3})/2$ (Fig. 4b) define the adjoint reciprocal lattice vectors $\mathbf{G}$. In the small angle limit, the relationship between the displacement $\mathbf{d}$ between layers (which characterizes local stacking) and position within the moiré pattern maps $\mathbf{G}$ onto the reciprocal lattice vectors $\tilde{\mathbf{G}}$ of the moiré cell via $\tilde{\mathbf{G}}(\theta, \mathbf{G}) \approx -\theta\hat{z} \times \mathbf{G}$ (Fig. 4c), with $\hat{z}$ the out-of-plane unit vector. We calculate phonon modes from local crystalline dynamical matrices $\bar{D}$ evaluated as a function of the displacement $\mathbf{d}$ (Fig. 4b). To calculate the optically active phonon modes near the central $\mathbf{\Gamma}$ point, we assemble the moiré dynamical matrix $\bar{D}_m(\mathbf{q}, \mathbf{q}')$ from matrices $\bar{D}(\mathbf{q}|\mathbf{d})$ evaluated for each local stacking $\mathbf{d}$ via Fourier transform,

$$\bar{D}_m(\mathbf{q}, \mathbf{q}') = \sum_{\mathbf{G},\mathbf{d}} \delta\left(\mathbf{q} - \mathbf{q}' - \tilde{\mathbf{G}}(\theta, \mathbf{G})\right) \bar{D}(\mathbf{q}'|\mathbf{d}) e^{i\mathbf{d}\cdot\mathbf{G}}. \quad (1)$$

This moiré dynamical matrix is off-diagonal in the reciprocal space variable $\mathbf{q}^{(\prime)}$ because of the slow spatial variation of $\mathbf{d}$. We find that small $|\mathbf{G}|$ terms dominate in equation (1), allowing us to truncate the sum after the first shell of six non-zero reciprocal lattice vectors, coupling each $\mathbf{q}$ point in the moiré reciprocal unit cell to six replicas. In particular, the central $\mathbf{\Gamma}$ point is coupled to six neighbours $\tilde{\mathbf{G}}_{1\ldots6}$ (blue dots in Fig. 4c). The $\bar{D}(\mathbf{q}|\mathbf{d})$ for each displacement $\mathbf{d}$ can be straightforwardly obtained from density functional perturbation theory. This model does not include any free parameters.

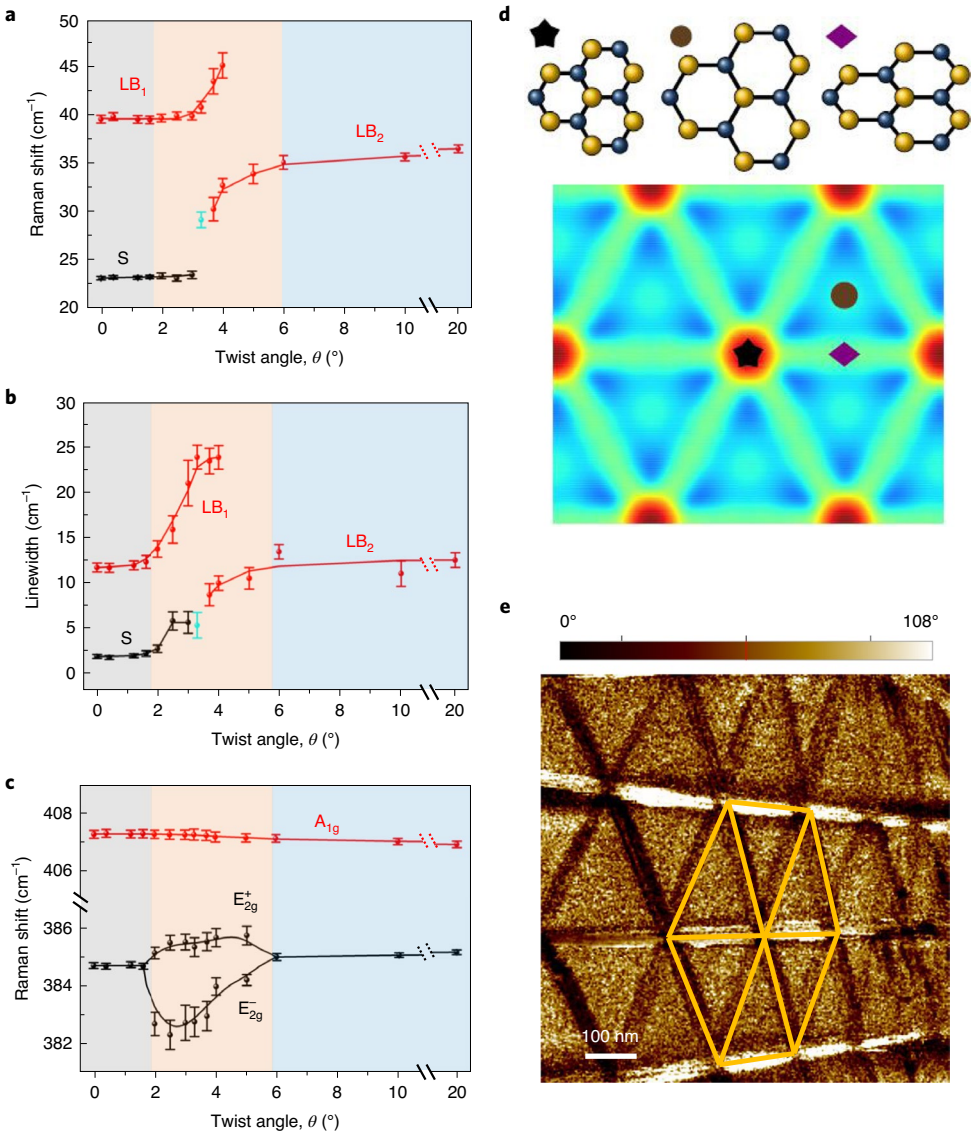

Fig. 3 | Analysis of the Raman spectra and experimentally observed lattice reconstruction. a,**b**, Central frequencies (**a**) and linewidths (**b**) of S, LB_1 and LB_2 as a function of the twist angle. The cyan dots in **a** and **b** refer to a mode that cannot be uniquely identified as LB or S. **c**, The central frequencies of intralayer modes as a function of twist angle. The error bars in **a**–**c** represent the uncertainty of the fitting parameter in the fitting process (Supplementary Discussion VI). **d**, Pictorial illustration of local strain at various positions within the moiré pattern: compressive at the AA (black star) stacking, tensile at AB (brown circle) stacking and uniaxial along the domain boundaries (violet diamond). The corresponding positions are indicated in the strain pattern of Fig. 1d. **e**, PFM phase image of reconstructed moiré superlattices at $\theta \approx 0.08°$.

When truncating the expansion after the first shell, our model yields a total of 126 modes, that is, 18 modes that are folded by the moiré reciprocal lattice and evolve continuously with twist angle. Mode energies calculated at the $\mathbf{\Gamma}$ point of MoS_2 probed by Raman spectroscopy, neglecting or including lattice relaxation, are shown in Fig. 4d or 4e, respectively. We rescale the overall interlayer coupling strength by a single factor of 1.15 to match the interlayer frequencies at $\theta = 0°$ to the experiment (Supplementary Discussion XI).

The LB modes are only weakly twist-angle dependent in both the relaxed ($LB_1 \approx 40\,cm^{-1}$) and the rigid ($LB_2 \approx 33\,cm^{-1}$) regimes (Fig. 4e). Calculations and measurements match perfectly for the LB modes at all θ. We find a prominent anticrossing of the LB modes caused by coupling to the dispersive folded transverse acoustic modes, in excellent agreement with the experimental evolution of the LB modes in the transition regime (Fig. 3a). At $\theta \approx 3.5°$, the folded transverse acoustic phonon modes originating at $\tilde{\mathbf{G}} = \tilde{\mathbf{G}}_1 \ldots \tilde{\mathbf{G}}_6$ (grey lines in Fig. 4d) are degenerate with the LB mode at $\mathbf{q} = \mathbf{\Gamma}$. The ultra-strong coupling between the two modes can be explained by the large $\mathbf{d}$ dependence of $\bar{D}(\mathbf{q}'|\mathbf{d})$ in the corresponding spacial direction. By comparing calculations without (Fig. 4d) and with (Fig. 4e) lattice relaxations, one recognizes that the LB modes are similar in both cases. Thus, although the rapid evolution of the LB modes coincides with the transition regime, our calculations suggest that this is not caused by the atomic reconstructions of the moiré pattern.

Only when accounting for relaxation of the lattice via elasticity theory (Fig. 4e and Supplementary Discussions I and XI (section C)), the instability (for example, imaginary frequency for the S mode) of the rigid TBLs for $\theta \lesssim 4°$ is removed. At small twist angles, lattice reconstruction causes the degenerate S mode frequencies to shift and match the measured values. For larger angles, our model overestimates the corrugation (variation of layer separation in **d**)

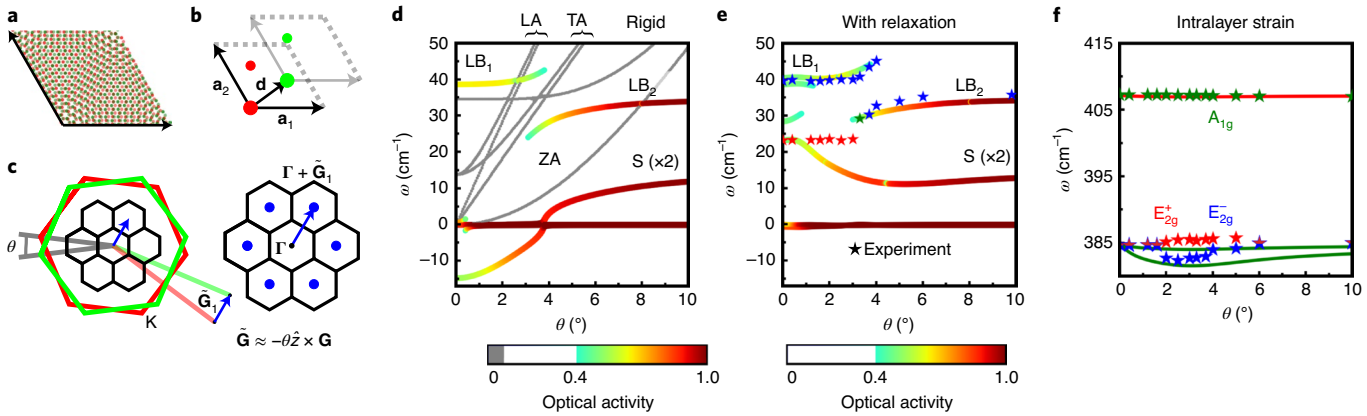

Fig. 4 | Calculated evolution of phonon modes as a function of twist angle θ. **a**, Real space representation of MoS_2 TBL at $\theta = 3.9°$. Atoms of the top (bottom) layer are illustrated in green (red). **b**, Locally stacked pristine unit cells. **c**, Reciprocal representation of the moiré Brillouin zone (central black hexagons) and its relation to the pristine Brillouin zones (green and red). Blue arrows indicate relation to neighbouring moiré $\mathbf{\Gamma}$ points. **d**,**e**, Low-energy phonon evolution at $\mathbf{q} = \mathbf{\Gamma}$, neglecting (**d**) or including (**e**) lattice relaxation as a function of twist angle θ. The deviations of the S mode at intermediate twist angles are discussed in detail in Supplementary Discussion X. Colour codes are based on optical activity (colour bar) as approximated by projecting the phonon eigenmodes $\mathbf{Q}_i$ onto the central $\mathbf{\Gamma}$ point, $|\langle \mathbf{Q}_i | \mathbf{\Gamma} \rangle|^2$. Grey lines in **d** show optically inactive modes entirely originating at neighbouring moiré $\mathbf{\Gamma}$ points (blue dots in **c**). TA, transverse acoustic; LA, longitudinal acoustic; ZA, out-of-plane acoustic; ×2 indicates the degeneracy of the S mode. **f**, Twist-angle-dependent evolution of the optical phonon modes A_{1g} (red line) and the degeneracy lifted $E^{\pm}_{2g}$ modes (green line). Stars in **e** and **f** indicate the corresponding experimental values. Calculated optical mode energies are shifted to match the experimental values at $\theta = 0°$.

of the moiré pattern[24], causing deviations between the calculated and measured S mode frequencies (Supplementary Discussion X). Neglecting its atomistic structure, the moiré patterns preserve C_3 symmetry even in the presence of lattice relaxation and therefore conserve the degeneracy of the S mode at the $\mathbf{\Gamma}$ point present for $\theta = 0°$. Given the complex interplay of layer separation, mode coupling and lattice reconstruction, a detailed explanation for the behaviour of the linewidth is outside the scope of the present work.

We also calculate the evolution of the A_{1g} and E_{2g} Raman peaks with twist angle. While the optically active A_{1g} mode is hardly affected by the moiré, local strain lifts the degeneracy of the E_{2g} mode by breaking the hexagonal symmetry[39,40]. The non-uniform strain present in moiré structures (Fig. 1c–e) becomes uniaxial at the domain walls (Fig. 3d), breaking the single-layer D_{3h} symmetry and causing splitting of the E_{2g} mode into $E^{\pm}_{2g}$ (ref. [39]). The observed proportionality between the splitting $E^{+}_{2g} - E^{-}_{2g}$ (Fig. 4f) and the average strain (Fig. 1f) further corroborates our model and underpins the crucial role of strain in these systems.

Summary and outlook

In summary, our study reveals that phonon spectra are renormalized in reconstructed MoS_2 moiré superlattices. We discover three regimes of atomic reconstructions characterized by distinct Raman spectra. We anticipate that these regimes and the phonon renormalization will occur in other TBLs although the range of the twist angle could vary. The most interesting Raman spectral changes in the transition regime suggest a continuous and subtle evolution of atomic configurations and strain. Such information is partially accessible via scanning tunnelling microscopy[14] but challenging for many common scanning probe and near-field techniques. In the same regime, a rich variety of electronic phases in TMD TBLs have been reported[13], highlighting the importance of reconciling electronic phases with static and dynamic lattice properties. To treat the phononic and electronic degrees of freedom on an equal footing, we introduce a computationally efficient method to describe phonons in moiré crystals at any small twist angle, which can be extended to describe electron–phonon interaction in the future. Thus, our work is also a necessary step towards addressing the influence of electron–phonon interactions on the Wigner crystal state stability[9], magnetic order[10] and metal–insulator transitions[13] in TMD moiré materials.

Online content

Any methods, additional references, Nature Research reporting summaries, source data, extended data, supplementary information, acknowledgements, peer review information; details of author contributions and competing interests; and statements of data and code availability are available at https://doi.org/10.1038/s41563-021-00960-1.

Received: 12 May 2020; Accepted: 16 February 2021;
Published online: 22 March 2021

References

1. Zhang, C. et al. Interlayer couplings, moiré patterns, and 2D electronic superlattices in MoS_2/WSe_2 hetero-bilayers. *Sci. Adv.* **3**, e1601459 (2017).
2. Tran, K. et al. Evidence for moiré excitons in van der Waals heterostructures. *Nature* **567**, 71–75 (2019).
3. Kim, K. et al. van der Waals heterostructures with high accuracy rotational alignment. *Nano Lett.* **16**, 1989–1995 (2016).
4. Cao, Y. et al. Unconventional superconductivity in magic-angle graphene superlattices. *Nature* **556**, 43–50 (2018).
5. Yankowitz, M. et al. Tuning superconductivity in twisted bilayer graphene. *Science* **363**, 1059–1064 (2019).
6. Sharpe, A. L. et al. Emergent ferromagnetism near three-quarters filling in twisted bilayer graphene. *Science* **365**, 605–608 (2019).
7. Serlin, M. et al. Intrinsic quantized anomalous hall effect in a moiré heterostructure. *Science* **367**, 900–903 (2020).
8. Cao, Y. et al. Correlated insulator behaviour at half-filling in magic-angle graphene superlattices. *Nature* **556**, 80–84 (2018).
9. Regan, E. C. et al. Mott and generalized Wigner crystal states in WSe_2/WS_2 moiré superlattices. *Nature* **579**, 359–363 (2020).
10. Tang, Y. et al. Simulation of Hubbard model physics in WSe_2/WS_2 moiré superlattices. *Nature* **579**, 353–358 (2020).
11. Shimazaki, Y. et al. Strongly correlated electrons and hybrid excitons in a moiré heterostructure. *Nature* **580**, 472–477 (2020).
12. Naik, M. H. & Jain, M. Ultraflatbands and shear solitons in moiré patterns of twisted bilayer transition metal dichalcogenides. *Phys. Rev. Lett.* **121**, 266401 (2018).
13. Wang, L. et al. Correlated electronic phases in twisted bilayer transition metal dichalcogenides. *Nat. Mater.* **19**, 861–866 (2020).
14. Gadelha, A. C. et al. Localization of lattice dynamics in low-angle twisted bilayer graphene. *Nature* **590**, 405–409 (2021).

15. Carr, S. et al. Relaxation and domain formation in incommensurate two-dimensional heterostructures. *Phys. Rev. B* **98**, 224102 (2018).
16. Sushko, A. et al. High resolution imaging of reconstructed domains and moiré patterns in functional van der Waals heterostructure devices. Preprint at https://arXiv.org/abs/1912.07446 (2019).
17. Weston, A. et al. Atomic reconstruction in twisted bilayers of transition metal dichalcogenides. *Nat. Nanotechnol.* **15**, 592–597 (2020).
18. McGilly, L. J. et al. Visualization of moiré superlattices. *Nat. Nanotechnol.* **15**, 580–584 (2020).
19. Jung, J., DaSilva, A. M., MacDonald, A. H. & Adam, S. Origin of band gaps in graphene on hexagonal boron nitride. *Nat. Commun.* **6**, 6308 (2015).
20. Rosenberger, M. R. et al. Twist angle-dependent atomic reconstruction and moiré patterns in transition metal dichalcogenide heterostructures. *ACS Nano* **14**, 4550–4558 (2020).
21. Yoo, H. et al. Atomic and electronic reconstruction at the van der Waals interface in twisted bilayer graphene. *Nat. Mater.* **18**, 448–453 (2019).
22. Zhang, K. & Tadmor, E. B. Structural and electron diffraction scaling of twisted graphene bilayers. *J. Mech. Phys. Solids* **112**, 225–238 (2018).
23. Alden, J. S. et al. Strain solitons and topological defects in bilayer graphene. *Proc. Natl Acad. Sci. USA* **110**, 11256–11260 (2013).
24. Huang, S. et al. Low-frequency interlayer Raman modes to probe interface of twisted bilayer MoS_2. *Nano Lett.* **16**, 1435–1444 (2016).
25. Nam, N. N. & Koshino, M. Lattice relaxation and energy band modulation in twisted bilayer graphene. *Phys. Rev. B* **96**, 075311 (2017).
26. Molina-Sánchez, A. & Wirtz, L. Phonons in single-layer and few-layer MoS_2 and WS_2. *Phys. Rev. B* **84**, 155413 (2011).
27. Tan, P. et al. The shear mode of multilayer graphene. *Nat. Mater.* **11**, 294–300 (2012).
28. Zhang, X. et al. Raman spectroscopy of shear and layer breathing modes in multilayer MoS_2. *Phys. Rev. B* **87**, 115413 (2013).
29. Zhao, Y. et al. Interlayer breathing and shear modes in few-trilayer MoS_2 and WSe_2. *Nano Lett.* **13**, 1007–1015 (2013).
30. Lin, M.-L. et al. Cross-dimensional electron-phonon coupling in van der Waals heterostructures. *Nat. Commun.* **10**, 2419 (2019).
31. Lee, C. et al. Anomalous lattice vibrations of single- and few-layer MoS_2. *ACS Nano* **4**, 2695–2700 (2010).
32. Verble, J. L. & Wieting, T. J. Lattice mode degeneracy in MoS_2 and other layer compounds. *Phys. Rev. Lett.* **25**, 362–364 (1970).
33. Li, H. et al. From bulk to monolayer MoS_2: evolution of Raman scattering. *Adv. Funct. Mater.* **22**, 1385–1390 (2012).
34. Puretzky, A. A. et al. Twisted $MoSe_2$ bilayers with variable local stacking and interlayer coupling revealed by low-frequency Raman spectroscopy. *ACS Nano* **10**, 2736–2744 (2016).
35. Holler, J. et al. Low-frequency Raman scattering in WSe_2–$MoSe_2$ heterobilayers: evidence for atomic reconstruction. *Appl. Phys. Lett.* **117**, 013104 (2020).
36. Liao, M. et al. Precise control of the interlayer twist angle in large scale MoS_2 homostructures. *Nat. Commun.* **11**, 2153 (2020).
37. Debnath, R. et al. Evolution of high-frequency Raman modes and their doping dependence in twisted bilayer MoS_2. *Nanoscale* **12**, 17272–17280 (2020).
38. Cuscó, R., Gil, B., Cassabois, G. & Artús, L. Temperature dependence of Raman-active phonons and anharmonic interactions in layered hexagonal BN. *Phys. Rev. B* **94**, 155435 (2016).
39. Lee, J.-U. et al. Strain-shear coupling in bilayer MoS_2. *Nat. Commun.* **8**, 1370 (2017).
40. Wang, Y., Cong, C., Qiu, C. & Yu, T. Raman spectroscopy study of lattice vibration and crystallographic orientation of monolayer MoS_2 under uniaxial strain. *Small* **9**, 2857–2861 (2013).
41. Lin, M.-L. et al. Moiré phonons in twisted bilayer MoS_2. *ACS Nano* **12**, 8770–8780 (2018).
42. Koshino, M. & Son, Y.-W. Moiré phonons in twisted bilayer graphene. *Phys. Rev. B* **100**, 075416 (2019).
43. Campos-Delgado, J., Cançado, L. G., Achete, C. A., Jorio, A. & Raskin, J.-P. Raman scattering study of the phonon dispersion in twisted bilayer graphene. *Nano Res.* **6**, 269–274 (2013).
44. He, R. et al. Observation of low energy Raman modes in twisted bilayer graphene. *Nano Lett.* **13**, 3594–3601 (2013).
45. Cocemasov, A. I., Nika, D. L. & Balandin, A. A. Phonons in twisted bilayer graphene. *Phys. Rev. B* **88**, 035428 (2013).
46. Jorio, A. & Cançado, L. G. Raman spectroscopy of twisted bilayer graphene. *Solid State Commun.* **175**, 3–12 (2013).
47. Maity, I., Naik, M. H., Maiti, P. K., Krishnamurthy, H. & Jain, M. Phonons in twisted transition-metal dichalcogenide bilayers: ultrasoft phasons and a transition from a superlubric to a pinned phase. *Phys. Rev. Res.* **2**, 013335 (2020).
48. Cocemasov, A. I., Nika, D. L. & Balandin, A. A. Phonons in twisted bilayer graphene. *Phys. Rev. B* **88**, 035428 (2013).
49. Jung, J., Raoux, A., Qiao, Z. & MacDonald, A. H. *Ab initio* theory of moiré superlattice bands in layered two-dimensional materials. *Phys. Rev. B* **89**, 205414 (2014).
50. Bistritzer, R. & MacDonald, A. H. Moiré bands in twisted double-layer graphene. *Proc. Natl Acad. Sci. USA* **108**, 12233–12237 (2011).

Publisher's note Springer Nature remains neutral with regard to jurisdictional claims in published maps and institutional affiliations.

© The Author(s), under exclusive licence to Springer Nature Limited 2021, corrected publication 2021

Methods

Sample preparation. The samples were fabricated using a modified tear-and-stack technique[3]. A schematic diagram of the stacking process is presented in Supplementary Fig. 3a. The hBN and monolayer MoS_2 flakes were mechanically exfoliated from a bulk crystal onto a polydimethylsiloxane sheet. The hBN thickness was typically around 15 nm, measured by atomic force microscopy. The MoS_2 monolayer was identified by optical contrast spectroscopy and Raman spectroscopy. The bottom hBN was first transferred onto the Si/SiO_2 (90 nm) substrate and subsequently annealed at 500 °C for 10 h. The van der Waals force between hBN and the MoS_2 monolayer was used to tear a part off the monolayer flake at room temperature, which was transferred onto the hBN. The separated monolayer pieces were rotated by a specific angle and stacked together. The accuracy in controlling the twist angle was ~0.1°. Finally, the samples were annealed under ultrahigh vacuum (around 10^{-5} mbar) to enhance the coupling between two layers. To avoid possible rotations between the layers, a relatively low temperature (150 °C) and a short process time (2 h) was used for the annealing. We carefully checked the microscope images before and after annealing and found no rotations during the annealing for all samples (Supplementary Fig. 3b,c). The spatial uniformity of the optical properties of the TBLs was futher confirmed via low-frequency Raman mapping (Supplementary Fig. 4).

Raman measurement. Raman spectra were measured at room temperature using a Princeton Acton 7500i spectrometer equipped with a liquid-nitrogen-cooled charge-coupled detector, with a ×100 objective lens (numerical aperture, 0.90). BragGrate notch filters were used to reject the Rayleigh scattering down to 8 cm^{-1}. The excitation laser was a 532 nm (that is, 2.33 eV) continuous-wave laser from a Verdi V10. A grating with 1,200 lines mm^{-1} was used in the Raman measurements. An incident laser power of 0.2 mW was used to avoid sample heating. The excitation laser and collected Raman signal were collinearly polarized.

PFM measurements. In a PFM measurement, an a.c. bias is applied on the conductive tip to induce sample deformation through the piezoelectric effect. The amplitude and phase of vertical (out-of-plane) and horizontal (in-plane) deformations of the sample are recorded during the contact-mode scan, providing local information of the electromechanical response. The experiments were performed on a commercial atomic force microscope (XE-70 AFM, Park Systems). A lock-in amplifier (HF2LI, Zurich Instruments) was used to apply the a.c. bias (typically around 1 V) and demodulate the PFM signals. The radius of the cantilever probe (ANSCM-PT-10, App Nano) was less than 30 nm, and the force constant was ~1–5 N m^{-1}. For out-of-plane PFM, the first harmonic of the cantilever resonance (~80–90 kHz) was used for detection. For in-plane PFM, the third harmonic frequency (~320–330 kHz) was used for detection.

Density functional perturbation theory calculations. To build the low-energy continuum model, two types of density functional perturbation theory calculations are required. For the **q**-dependent parts of the moiré dynamical matrix we calculate one single layer of MoS_2 using a 6×6×1 supercell. For the **q**-independent part, we employ 10×10 individual primitive cell bilayer MoS_2 density functional perturbation theory calculations sampling the different stackings **d**. We use Vienna Ab-initio Simulation Package with a **k**-point Monkhorst–Pack grid of 17×17×1 (3×3×1 for the supercell) with an energy cut-off of 400 eV and a unit cell height of 35 Å to provide sufficient vacuum between the layers[51,52]. For simplicity we use the local density approximation (for further details see Supplementary Discussion XII).

Calculation of strain and lattice relaxation. Strain was calculated by minimizing the total energy functional,

$$U_{\mathrm{tot}} = U_{\mathrm{B}}[\mathbf{u}^t, \mathbf{u}^b] + U_{\mathrm{E}}[\mathbf{u}^t] + U_{\mathrm{E}}[\mathbf{u}^b],$$

with respect to the top (t) and bottom (b) layer displacements $\mathbf{u}^{t/b}(\mathbf{r})$ at position **r**. We model the potential energy functional U_{B} via a generalized stacking fault energy[15,25] obtained from sampling the configuration space using density functional perturbation theory. The 2D elastic energy functional $U_{\mathrm{E}}[\mathbf{u}^{t(b)}]$ is modelled using the Lamé parameters $\lambda = 3.29$ eV Å^{-2} and $\mu = 3.6$ eV Å^{-2} (ref. [15]; for further details see Supplementary Discussion I).

Data availability

All relevant data are available from the authors upon reasonable request.

Code availability

All relevant codes are available from the authors upon reasonable request.

References

51. Kresse, G. & Hafner, J. *Ab initio* molecular dynamics for liquid metals. *Phys. Rev. B* **47**, 558–561 (1993).
52. Kresse, G. & Hafner, J. *Ab initio* molecular-dynamics simulation of the liquid-metal–amorphous-semiconductor transition in germanium. *Phys. Rev. B* **49**, 251–271 (1994).

Acknowledgements

The spectroscopy experiments at the University of Texas at Austin (J.Q.) were primarily funded by the US Department of Energy, Office of Basic Energy Sciences under grant DE-SC0019398 and a grant from the University of Texas. Material preparation was funded by the Welch Foundation via grant F-1662. The collaboration between the X.L., C.-K.S., K.L. and A.H.M. groups is facilitated by the National Science Foundation Materials Research Science and Engineering Centers (MRSEC) under DMR-1720595, which funded J.C. and J.E. partially. L.L. and F.L. acknowledge support by the TU-D doctoral programme of TU Wien, as well as from the Austrian Science Fund (FWF), project I-3827, and L.L. acknowledges additional support from the Austrian Marshall Plan Foundation. We acknowledge discussions with S. Reichardt and the use of facilities and instrumentation supported by the National Science Foundation through the Center for Dynamics and Control of Materials and National Science Foundation MRSEC under cooperative agreement no. DMR-1720595. P.-H.T. and M.-L.L. acknowledge support from the National Natural Science Foundation of China (grant nos 12004377 and 11874350), CAS Key Research Program of Frontier Sciences (grant no. ZDBS-LY-SLH004) and China Postdoctoral Science Foundation (grant no. 2019TQ0317). The PFM work (D.L. and K.L.) was supported by National Science Foundation DMR-2004536 and Welch Foundation grant F-1814. X.L. gratefully acknowledges the support of sample preparations from the Welch Foundation via grant F-1662. K.W. and T.T. acknowledge support from the Elemental Strategy Initiative conducted by the MEXT, Japan, grant no. JPMXP0112101001; JSPS KAKENHI, grant no. JP20H00354; and the CREST(JPMJCR15F3), JST.

Author contributions

J.Q. led the optical experiments, and M.-L.L., C.-Y.W., W.-T.H., J.E. and J.C. assisted with the experiment. L.L. led the theoretical calculations, and J.Z. contributed to the theoretical discussions. D.L. performed the PFM measurements. J.Q. and C.Y. prepared the TBL samples. T.T. and K.W. provided the hBN sample. J.Q., L.L., F.L. and X.L. wrote the manuscript. X.L., F.L., A.H.M., P.-H.T., K.L. and C.-K.S. supervised the project. All authors discussed the results.

Competing interests

The authors declare no competing interests.

Additional information

Supplementary information The online version contains supplementary material available at https://doi.org/10.1038/s41563-021-00960-1.

Correspondence and requests for materials should be addressed to P.-H.T., F.L. or X.L.

Peer review information *Nature Materials* thanks the anonymous reviewers for their contribution to the peer review of this work.

Reprints and permissions information is available at www.nature.com/reprints.